

<https://doi.org/10.1038/s43246-025-01053-1>

Quasi-2D gallium oxide X-ray detector

Check for updates

Ruo-fan Li^{1,2}, Chen Hua^{1,2}, Xue-qing Chen^{1,2}, Zhong-shan Deng^{1,2}, Ming-hui Guo¹, Qian Li¹✉ & Jing Liu^{1,2}✉

X-rays, characterized by their short wavelength and high penetrating power, are indispensable across numerous fields. Current X-ray detection relies heavily on amorphous selenium (a-Se) and medium bandgap semiconductors (e.g., Si, CdTe, CZT), which often face limitations including complex large-scale fabrication, high cost, and stability issues under intense irradiation. While alternative wide-bandgap materials like diamond offer excellent performance, challenges related to scalable fabrication and cost often remain. Here, we report a high-performance X-ray detector based on solution-processed quasi-two-dimensional (2D) gallium oxide (Ga₂O₃) films fabricated via a novel liquid metal nano-printing technique. Leveraging the ultra-wide bandgap and high quality of the printed Ga₂O₃, the device achieves an ultra-high sensitivity of 6050 μC/Gy/cm². We further demonstrate the practical utility of these detectors by integrating them into a functional X-ray imaging system. This work establishes liquid metal nano-printing as a vital pathway for the rapid fabrication of ultrathin, high-performance, low-power-consumption X-ray detectors. Additionally, this work enables low-dose, high-resolution X-ray imaging for medical diagnostics and non-destructive testing, demonstrating a cost-effective pathway toward portable radiation detection systems.

X-rays are electromagnetic waves with extremely short wavelengths and strong penetrating ability, which have been widely used in the fields of industrial nondestructive testing, medical imaging and radiation therapy, security systems and aerospace^{1–5}. The growing demand for X-ray detectors is putting forward higher performance requirements from the early days of film, calorimetry and other traditional detection methods, to the gradually developed pyroelectricity, glow exhaustion fluorescence, scintillator and other indirect detection technology and direct detection technology such as ionization chambers. The commonly used X-ray detectors can be roughly divided into three categories according to their different working mechanisms: gas detectors, scintillator detectors and semiconductor detectors^{6–8}.

Gas X-ray detectors were used more often in the early days of high-energy irradiation detection in outer space. However, the bulky shape of gas detectors made it more difficult to mount satellites; therefore have been gradually replaced in recent years. Recent breakthroughs in scintillator materials have expanded the design paradigms for X-ray detection. For instance, ZnO quantum dot glass scintillators achieve 96% transparency at meter-scale dimensions, enabling low-dose imaging (37.6 nGy/s) via triplet self-trapping exciton engineering⁹. Meanwhile, perovskite-based 3D/0D heterostructures (e.g., Cs₂NaLuCl₆/Cs₃LuCl₆) generate color-integrated white light through controlled charge transfer, improving imaging contrast

by fivefold compared to conventional CsI:TI¹⁰. Notably, manganese halide glass-ceramics (Al₄B₂O₉: MnBr₂) maintain zero thermal quenching at extreme temperatures by leveraging low-phonon Mn-Br polyhedra, highlighting pathways toward multifunctional detection in harsh environments¹¹. In recent years, novel ultra-wide-bandgap semiconductor X-ray detectors^{12–14} have attracted renewed industrial attention for next-generation applications, complementing established direct detection technologies such as Li-doped Si and diamond because of their excellent response characteristics, good digital signal compatibility, and resistance to irradiation. The commonly used direct-type X-ray detection materials include amorphous Se, PbI₂, HgI₂, CdTe, CdZnTe and PbO^{15–20}. These materials all contain elements with large atomic numbers, which increase the scattering cross section of the material interacting with X-rays and increase the absorption efficiency of X-rays^{21,22}. Recent advances in direct detection materials have expanded the toolkit for X-ray imaging. Perovskite quantum dots are currently highly favored in the field of direct X-ray detection, with reports already documenting their application in flat panel detectors²³. Newly developed semiconductors containing stable selenium cations, [(CH₃CH₂)₃S]₆Bi₈I₃₀ and [(CH₃CH₂)₃S]AgBiI₅, have been used in X-ray detection applications to produce detectors with excellent sensitivity and low detection limits²⁴. Meanwhile, diamond films with engineered color centers (e.g., NV⁻) achieve sub-pixel resolution through charge-sharing

¹State Key Laboratory of Cryogenic Science and Technology, Technical Institute of Physics and Chemistry, Chinese Academy of Sciences, Beijing, China. ²School of Future Technology, University of Chinese Academy of Sciences, Beijing, China. ✉e-mail: liqian@mail.ipc.ac.cn; jliu@mail.ipc.ac.cn

localization, and their exceptional radiation hardness suits extreme-environment applications^{25,26}.

Although these materials exhibit high X-ray absorption efficiency, their narrow bandgap imposes significant limitations: pronounced thermal effects, weak radiation resistance, high sensitivity to ambient temperature, and susceptibility to performance degradation under intense irradiation. Furthermore, their fabrication processes feature narrow windows, complex workflows, and high costs. The use of bulk material increases overall device bulkiness, compromising compatibility with modern flexible electronics. This makes them ill-suited for detecting flexible, portable, or irregularly shaped objects and hinders integration into next-generation electronic devices. How to break through the limitations of traditional materials and realize miniaturized high-performance new X-ray detectors is an urgent problem to be solved. The new nanoscale semiconductors represented by 2D materials and the disruptive photodetection technology formed by them have exceeded the theoretical limits of traditional thin-film devices in terms of detection sensitivity, very low dark current, and many other indicators, and are one of the strong contenders for developing the next generation detection technology. In addition, as compared to large-volume bulk structures that are mature in the fabrication process, the use of ultrathin-film device structures to reduce device size, expand device integrability and cost savings is a core topic yet to be explored. Gallium oxide (Ga_2O_3), as an ultra-wide bandgap semiconductor material (bandgap width 4.6–5.3 eV), has demonstrated significant potential in X-ray detection in recent years. Its ultra-wide bandgap, high breakdown field strength (8 MV/cm), high X-ray absorption coefficient (due to high density, 6.44 g/cm³), and high-temperature resistance make it a high-sensitivity material suitable for fabricating X-ray detectors whether in single-crystal or thin-film phases^{27,28}. With an average atomic number of 17.2, Ga_2O_3 has a higher atomic number than ZnO and GaN, and its absorption efficiency for hard X-rays is one order of magnitude higher than that of materials such as SiC and diamond. In addition, based on the compound luminescence of free electrons and self-trapped holes, Ga_2O_3 has an extremely fast (less than 10 ns) decay time^{29,30}. However, up to now, the research work on the X-ray detection properties and anti-irradiation characteristics of Ga_2O_3 materials is relatively small. In our understanding, no Ga_2O_3 -based X-ray detectors have been reported for imaging so far, so there is an urgent need to carry out research on Ga_2O_3 -based X-ray detectors, disclose their potential for X-ray imaging and fill the relevant gaps.

In this work, we proposed to introduce the quasi-2D Ga_2O_3 in X-ray detection, employing ultrathin 2D Ga_2O_3 as the core semiconductor of the detector. We construct quasi-2D Ga_2O_3 X-ray detectors by a novel low-cost liquid metal nano-printing process, investigate the response mechanism of Ga_2O_3 to X-ray irradiation, and reveal the working principle of the detectors. Owing to the high-quality quasi-2D ultrathin Ga_2O_3 film, the detector exhibits excellent stability and good detection performance for strong and weak light, and the sensitivity of the device to X-rays with an energy of 20 keV is as high as 6050 $\mu\text{C}\cdot\text{cm}^{-2}\text{Gy}^{-1}$ under a bias voltage of 10 V, originates from direct charge collection without intermediate scintillation steps, while the nano-printing fabrication ensures thickness control at atomic scales for high spatial resolution. Further, we fabricated a large-area amorphous quasi-2D Ga_2O_3 X-ray detector array and developed its prototype for high-resolution imaging applications.

Compared to traditional preparation methods, our approach offers multiple revolutionary advantages: our technical solution is fully compatible with modern microelectronics processes and possesses the potential for mass production. The low-temperature fabrication process enables deposition of our detectors onto diverse substrates, including glass, plastic, and even paper, paving the way for ultra-thin, portable, and even flexible X-ray imaging detectors. This holds significant importance for specialized applications such as dose monitoring in synchrotron radiation facilities and nuclear power plants. Through these innovations, our work aims to overcome multiple limitations of conventional X-ray detectors, paving a new path for the development of next-generation high-performance, low-cost, flexible X-ray detection technology.

Results and discussion

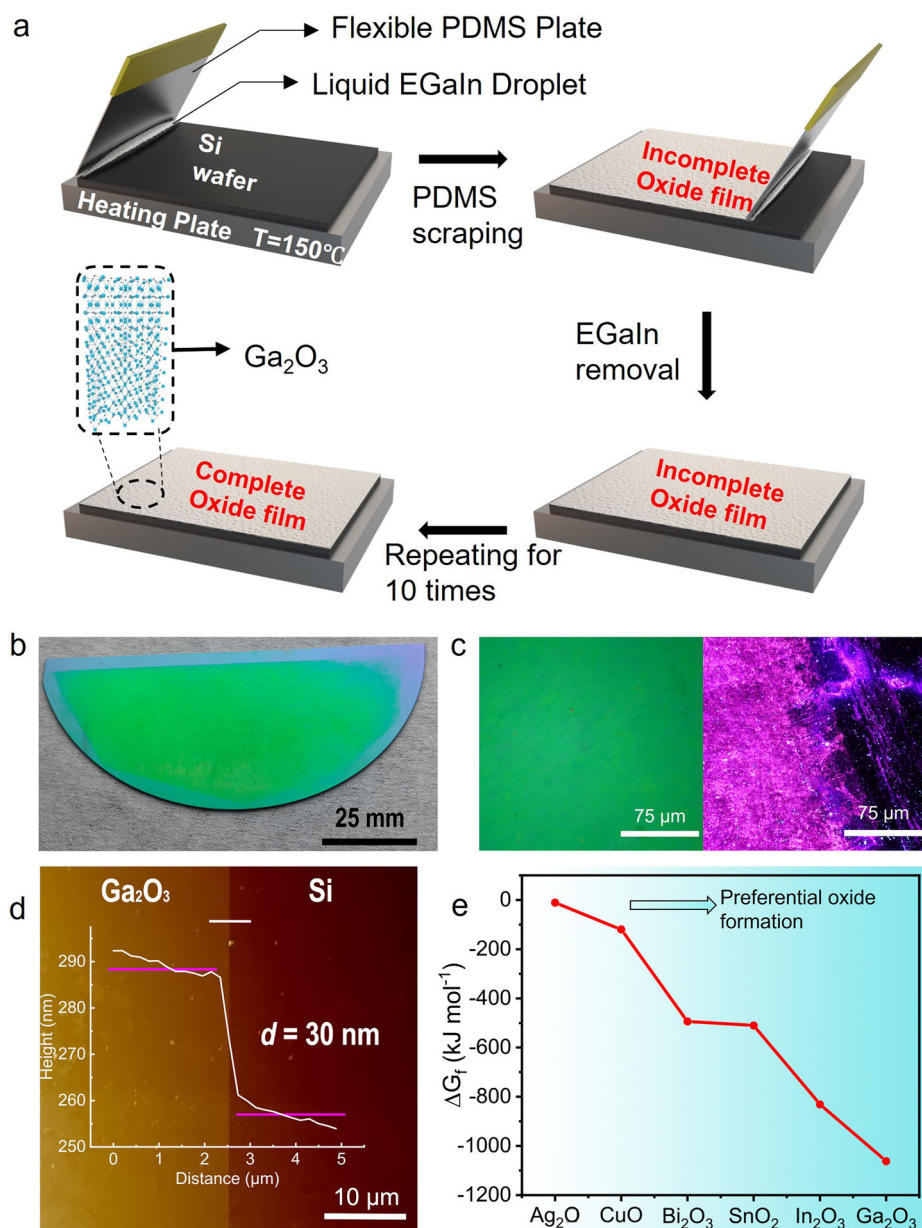
Direct printing of liquid metal-based quasi-2D Ga_2O_3

Up to now, the preparation techniques of semiconductor thin films have been widely reported, including MOCVD³¹, HVPE³², CVD³³, RF sputtering³⁴, squeeze printing³⁵, etc. However, the thin film semiconductors obtained based on these techniques always fail to satisfy the three advantages, namely, large area, good homogeneity, and low manufacturing temperature simultaneously. We established a process for the preparation of quasi-2D Ga_2O_3 semiconductor thin films by liquid metal nano-printing process, and the flow chart of this preparation process is shown in Fig. 1a. First, we subjected the surface of single-crystal silicon wafers to an oxygen plasma treatment to increase the surface electron concentration and enhance its affinity for contacting with the liquid metal droplets, and the silicon wafers were fixed on a heating plate after the plasma treatment, and the temperature was raised to 150 °C. The liquid eutectic gallium indium metal (Ga 75.5%, In 24.5% wt.) drops on the silicon wafer, we adopted a flexible Polydimethylsiloxane (PDMS) squeegee to roll droplets on the substrate (The PDMS substrate is uniquely suited for liquid metal nano-printing due to its ultra-low surface energy (21 mN/m) and optimal elastic modulus (1.5–2.5 MPa). While limited alternatives exist within strict property bounds ($\gamma \leq 25$ mN/m, $E = 0.5$ –5 MPa)—such as Ecoflex or FEP—most flexible polymers (e.g., PET, PI) are incompatible. Substrates beyond these thresholds induce print failure via film rupture or interfacial locking), effectively printing the droplet squeegee into a uniform film. Since there are no covalent bonds between Ga and Ga_2O_3 , there is a minimum interaction between the Ga_2O_3 and the liquid metal. As a result, quasi-2D amorphous Ga_2O_3 can be obtained on SiO_2/Si substrates considering the powerful van der Waals forces. It should be noted that a single printing process does not ensure that the oxide film is uniformly deposited on the silicon wafer surface, so multiple repetitions of printing are required to achieve uniform deposition of the oxide film. At the same time, in order to avoid mutual interference between each printing cycle, the end of each printing cycle must be used to clean the wafer surface with alcohol cotton to ensure that there is no liquid EGaIn residue. During the cleaning process, due to the strong van der Waals force adhesion between the oxide film and the substrate, the oxide film will always be firmly attached to the wafer surface. On the other hand, liquid EGaIn weakly binds to the deposited oxide film and can be easily removed by wiping, allowing the deposited oxide film to be cleaned without any damage. This preparation process owns the advantages of easy manufacturing, low cost, arbitrarily adjustable size and controllable thickness, which it provides a new pathway for the efficient and low-cost preparation of low-dimensional materials. We compared it with the conventional process in terms of preparation scale, homogeneity and manufacturing temperature, as shown in Supplementary Fig. 1.

The reaction principle of the printing process follows the Cabrera–Mott oxidation model, where surface oxides can spontaneously form on liquid metal surfaces in the surrounding atmosphere and other oxygen-containing environments, and after the formation of the initial oxide layer, electrons from the body of the metal adsorb oxygen from the surface through a tunneling process that creates a gradient of electric field across the oxide layer. This electric field, defined by the work function of the metal and ionized oxygen (Mott field), drives the migration of ions into the oxide layer, thus promoting growth. As the oxide layer becomes thicker, the magnetic field strength decreases, leading to self-termination of this process, with a final oxide thickness of a few nanometers, so that the growth of surface oxides is a self-limiting reaction at low to medium temperatures. In addition, the electron density distribution at the boundary between the liquid metal surface and the oxide is minimal, indicating the absence of covalent bonding. The non-polar nature of the liquid metal also limits non-covalent interactions, and the combination of these two effects results in weak adhesion of the natural surface oxide to its molten parent metal, so that this ultrathin oxide layer can be easily stripped onto the desired substrate. The process is relatively simple and efficient, enabling the synthesis of large areas of ultrathin materials with minimal defects. We took the photograph of printed Ga_2O_3 film at the macroscopic scale. As shown in Fig. 1b, the one

Fig. 1 | Schematic of the quasi 2D Ga₂O₃ printing process and morphological characterizations.

a Flow chart of the process of preparing Ga₂O₃ film by liquid metal printing method. **b** Photograph of a Ga₂O₃ film on a silicon substrate, in which the green part is the Ga₂O₃ film, and the violet substrate at the edges is the silicon substrate. **c** A Ga₂O₃ film under the metallographic microscope. The left image is the bright field, observing its surface uniformity and flatness, and the right image is the dark field, observing whether there are noise and defects on its surface. **d** AFM image at the step of the Ga₂O₃ film, showing its thickness of about 30 nm. **e** Schematic of standard formation Gibbs free energy change for common metals in liquid metal systems. The line between the formation energies indicates a guideline to the eye.



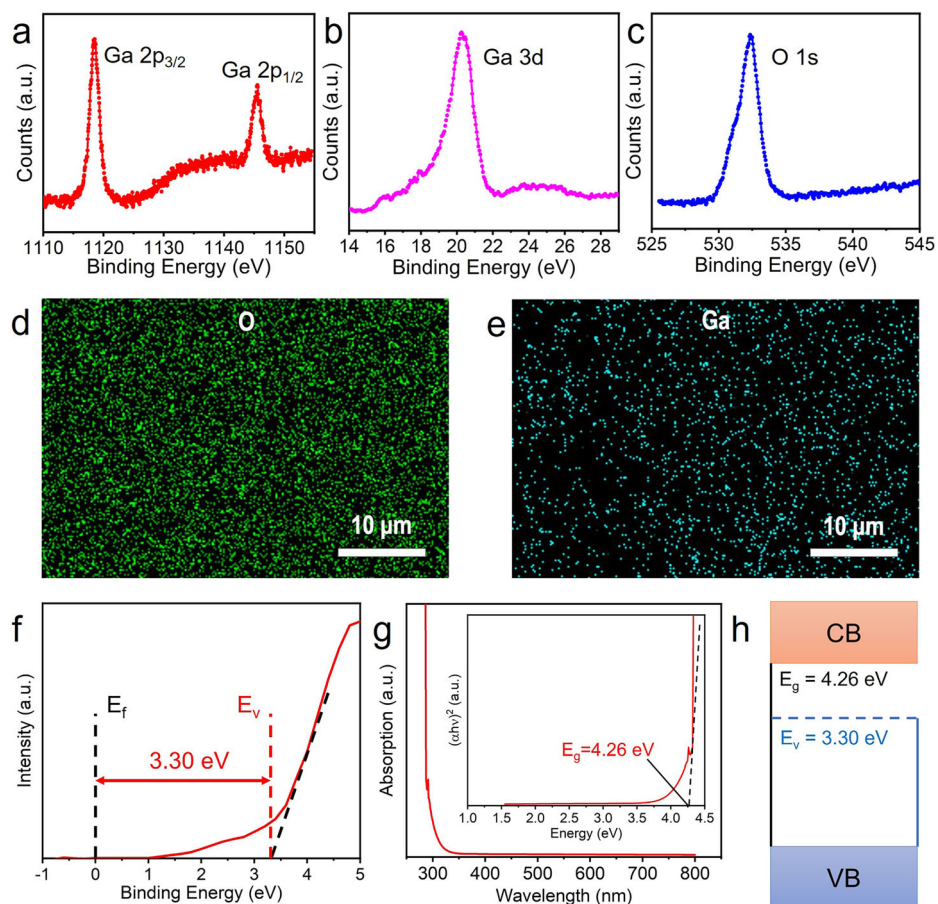
showing purple color is the silicon substrate, and the one indicating light green color is the printed Ga₂O₃ film. Our Ga₂O₃ film shows good flatness and homogeneity at the macro scale. We used metallographic microscope to better examine the surface flatness of the films. The photographs under metallographic microscope are shown in Fig. 1c. The left figure shows the bright-field observation of the Ga₂O₃. At 50 μm scale, it can be observed that the surface of the Ga₂O₃ film is smooth and dense without obvious scratches, defects, noises and other structures that affect the film performance, and the uniform color is also complementary to prove that the printed Ga₂O₃ has good flatness and integrity. The right figure is the image of the film steps under the dark-field metallographic microscope, it can be seen that the thickness uniformity at the film is good, and the junction between the film and the silicon wafer is obvious, and there is no thickness gradient, which fully explains the excellent uniformity and selectivity of the liquid metal printing process.

We measured the film thickness accurately by Atomic Force Microscope (AFM), and the results are shown in Fig. 1d. The film steps possess a 30 nm thickness mutation, which proves that the printed Ga₂O₃ film has a sharper thickness mutation at the edges with a height of 30 nm. We

measured the thickness of the films printed with different number of layers, and the data are shown in Supplementary Fig. 2. The measurements clearly show that the increase in Ga₂O₃ thickness decreases with the number of printings, showing to some extent the self-limiting thickness of the films. And this feature is crucial for 2D Ga₂O₃ film printing and processing, as the thickness limitation at the nanometer level confines the film to the realm of a two-dimensional material, which allows for restricted electron motion in the film, allowing for quantization of energy and better selectivity in response to light. Observation of the main part of the film inside the steps shows that the film thins out near the edges, but no abrupt changes are observed, and the slope of the thickness thinning is stable, which also indicates that the film possesses a good thickness uniformity. Our printed Ga₂O₃ maintains nanometer-level thickness (no more than 30 nm) while the sample size is large, giving it a promising application. In order to observe the Ga₂O₃ film morphology in a different way, we also used TEM to observe the film, and the results are as follows Supplementary Fig. 3.

Figure 1e shows the standard formation Gibbs free energy change (ΔG_f), which indicates the activity of oxidation reaction of each common metals. As Fig. 1e shows, the ΔG_f of Ga₂O₃ is the lowest of these common

Fig. 2 | Material characterization of 2D Ga₂O₃. XPS analysis of Ga₂O₃ thin films, **a** Plot corresponds to the energy interval of 1110–1155 eV, **b** Plot corresponds to the energy interval of 14–29 eV, and **c** Plot corresponds to the energy interval of 525–545 eV. **d**, **e** EDS spectroscopy of Ga₂O₃ films depicting the composition of the films in the form of fluorescence pictures while showing their spatial distribution. **f** VB-XPS test plot of Ga₂O₃ film, which shows the valence band position. **g** Image of UV-Vis-NIR spectrophotometer, which shows the band gap of Ga₂O₃ film. **h** Schematic of Ga₂O₃ film band structure.



metals. This data indicates that Ga will be oxidized firstly in common liquid metal system in thermodynamic theory. The oxidation kinetics during liquid metal nano-printing follows a Cabrera–Mott mechanism³⁶, where interfacial electric fields drive cation diffusion through sub-nm oxide layers. While classical models assume isotropic oxide growth, anisotropic electron transfer at heterogeneous interfaces (e.g., liquid Ga/oxide) can locally alter ion mobility³⁷. This aligns with MD simulations showing thermal-force-dominated ion hopping across disordered oxide interfaces³⁸.

In order to verify the exact composition of the Ga₂O₃ films, we resorted to X-ray Photoelectron Spectroscopy (XPS) and Energy Dispersive Spectrometer (EDS) analysis. Figures 2a–c shows the photoelectron energy spectra of Ga2p orbitals, Ga3d orbitals and O1s orbitals, respectively. It can be seen that in Fig. 2a, about 1120 eV and 1145 eV show two distinct sharp peaks, and a review of the data indicates that these two absorption peaks correspond to the 2p orbitals of the Ga element. The left-right symmetrical spectral peaks identify the Ga element in the film as a compound, and the characteristic energy loss peak at 1130 eV excludes the In3d orbitals with similar characteristics, identifying the presence of compounds of the Ga element in the film, and the In element is not detected, which also confirms the order of generation of the oxide film analyzed in the previous section. The energy interval in Fig. 2b corresponds to the Ga3d orbitals, and it can be seen that the absorption peaks are a single unit without splitting, which also identifies the presence of Ga in the film as a compound rather than a monomer. The energy interval corresponding to Fig. 2c is the 1s orbital of O element, and its peak width is less than 5 eV, and this XPS feature identifies the presence of oxygen element in the film as a metal oxide rather than other forms such as carbonate, water, and organic matter. At the same time, the clear, symmetric peaks can be directly observed from the graph of the peak half-height width, this feature can also be identified that the oxygen element

exists on the surface of the film only in the form of metal oxides, which verifies that the main component of the oxide film is Ga₂O₃.

In order to determine the elemental composition of the synthesized samples, EDS elemental analysis was performed and Fig. 2d, e indicate the mapping of O and Ga elements, both of which can be clearly found in the signals of these two elements, and the signals of O elements are more intense due to the effect of the SiO₂/Si substrate. It also can be clearly seen that the spatial distribution of the elements O and Ga is very uniform, which also verifies that the homogeneity of the Ga₂O₃ film is very good from the elemental point of view, and that there are no defects such as agglomeration, film rupture, or excessive film thickness.

After verifying that the film consists of Ga₂O₃, we tested its crystalline form by X-ray diffraction (Supplementary Fig. 4) and Raman spectroscopy (Supplementary Fig. 5). The XRD test results show that the peaks of α -Ga₂O₃ and β -Ga₂O₃. Supplementary Fig. 4 shows the 110 and 510 crystal planes of β -Ga₂O₃ and the 0006 plane of α -Ga₂O₃. This result proves that the film contains α -Ga₂O₃ and β -Ga₂O₃ simultaneously, i.e., polycrystalline Ga₂O₃. In addition, we further verified the Ga₂O₃ crystal structure by Raman spectroscopy. The result is shown in Supplementary Fig. 5. The A1 (T₀) peak of Ga₂O₃ at 275 nm⁻¹ is shown clearly in the figure. However, the 565 nm⁻¹ peak of Ga₂O₃ is masked by the highest peak which is the peak of silicon. The test results of XRD and Raman spectroscopy together demonstrate the presence of both α -Ga₂O₃ and β -Ga₂O₃ in the film. Its solid-state physical properties also need to be tested to initially verify whether it has good solar-blind X-ray detection performance. First, VB-XPS was used to test the valence band position of the sample film to determine the distance between the top of the valence band and the Fermi energy level, and the results are shown in Fig. 2f. Taking the intersection of the tangent line and the baseline at the original curve is the value of the valence band

position, the result is 3.30 eV, which is a larger value relative to conventional semiconductors.

In order to verify the solar-blind performance of the film, an absorbance test is required. As shown in Fig. 2g, we adopted a UV–Vis–NIR spectrophotometer to perform the absorbance test, deriving the absorbance curve and calculating the absorbance versus photon energy curve. The intersection of the tangent line and the horizontal axis on the energy curve is the forbidden bandwidth of the film, and the measured data is 4.26 eV. This value is much larger than the maximum value of visible light energy, i.e., 3.11 eV, so the visible range of light is impossible to make Ga₂O₃ film produce electron jump. Based on the valence band position and forbidden bandwidth obtained from the test, the energy band structure of the Ga₂O₃ film can be schematically made, as shown in Fig. 2h. It can be seen that the Fermi energy level of the Ga₂O₃ film is closer to the bottom of the conduction band than to the top of the valence band, which predicts that it should be an N-type semiconductor.

Notably, the measured bandgap value is slightly lower than the conventional value for Ga₂O₃. We propose three explanations for this phenomenon. Firstly, high V_O concentrations create defect states 0.4–0.6 eV below the conduction band minimum, reducing the effective gap by up to 0.55 eV. This aligns with Density Functional Theory (DFT) studies showing each 1% oxygen deficiency lowers E_g by ~0.11 eV in Ga₂O₃³⁹. Additionally, liquid-metal-printed films contain metastable ε-Ga₂O₃ domains (distorted octahedral coordination) with intrinsically lower bandgaps (4.5–4.8 eV). Phase mixing explains an additional 0.25 eV reduction⁴⁰. Furthermore, at 20 nm thickness (near β-Ga₂O₃'s exciton Bohr radius of ~4 nm), weakened quantum confinement softens the band edge by 0.1–0.2 eV⁴¹. Collectively, these mechanisms—dominantly V_O defects, ε-phase coexistence and quantum confinement loss—account for the observed 0.6 eV reduction. This deviation is consistent with defect-engineered Ga₂O₃ synthesized via low-temperature solution processes.

Quasi-2D Ga₂O₃ X-ray detector devices

Based on the obtained high-quality quasi-2D Ga₂O₃ films, we have constructed a quasi-2D Ga₂O₃-based X-ray detector, clarified the absorption of X-rays and the ability of Ga₂O₃ films to perform photoelectric conversion, and validate the potential of this printed film for application in the field of X-ray detection. Figure 3a shows the schematic structure of the Ga₂O₃-based X-ray detector linear array. In order to realize the formation of a low-resistance and high-quality contact interface between Ga₂O₃ and the electrodes, Au is used as the electrode of the Ga₂O₃ detector, and a fork-finger electrode structure is adopted with a finger width of 100 μm and a finger spacing of 100 μm, and the whole electrode unit has a width of 4 mm and an electrode diameter of 1 mm, i.e., the size of a single. The fork-finger electrode structure allows sufficient light transmission necessary for the transparency requirement while simultaneously enhancing charge collection efficiency. The interdigitated geometry reduces the average carrier transit distance to the electrodes, minimizing recombination losses and thereby amplifying the detected photocurrent signal. The distance between two neighboring photodetector cells is 1.5 mm, which is significantly larger than the thickness of Ga₂O₃ (30 nm), mainly to avoid signal crosstalk caused by lateral diffusion of photogenerated carriers and light scattering at grain boundaries.

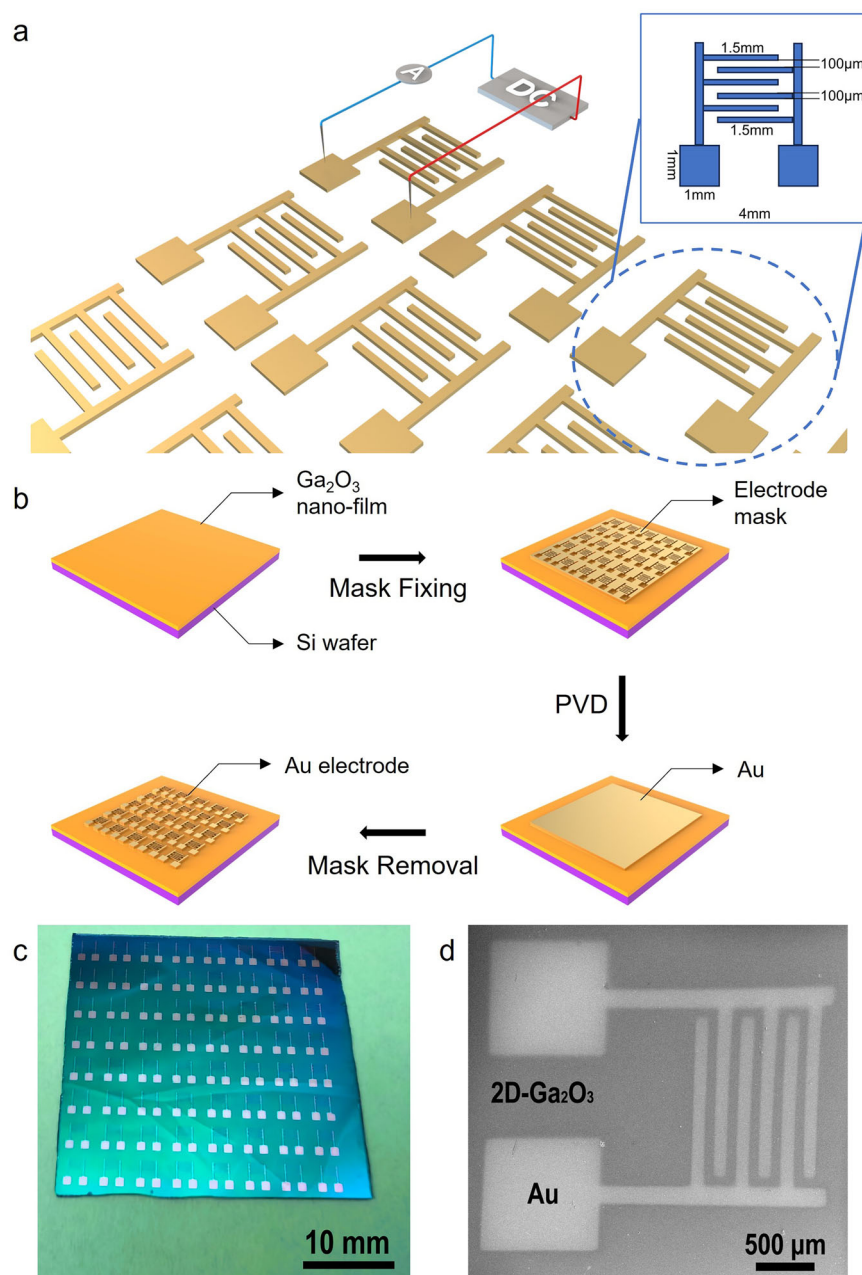
In order to ensure the processing accuracy of the detector devices, the Au electrodes were prepared by a magnetron sputtering process, and the flow chart of the whole device preparation is shown in Fig. 3b. A shadow mask with the desired electrode pattern was carefully aligned and placed in direct contact with the sample surface prior to loading into the sputter chamber. The chamber was evacuated to a base pressure of 0.08 mbar. High-purity Au was used as the target material. Prior to deposition, the target was pre-sputtered for 2 min in an Argon atmosphere at a pressure of 0.15 mbar to remove surface contaminants. The actual deposition was then performed under identical Ar pressure 0.15 mbar at a DC current of 20 mA for a duration of 300 s. This process resulted in a uniform metal electrode layer with a thickness of 20 nm. The shadow mask ensured the precise definition of the electrode geometry without requiring subsequent lithography and

etching steps. Photographs of the X-ray detector array are shown in Fig. 3c. The device contains 64 photodetector cells, each of which consists of a single Metal-Semiconductor-Metal (MSM) structured detector. SEM was used to observe the device microscopic morphology in more detail, as shown in Fig. 3d, the demarcation line between the electrode and the Ga₂O₃ film is obvious, and the electrode has a clear contour, uniform morphology and high surface flatness.

We have investigated a range of photoelectric properties of a quasi-2D Ga₂O₃-based X-ray detector line array. Figure 4a shows the system schematic of X-ray detection, the I–V curve and responsivity test in the X-ray shielding room, and the ray tube is made of tungsten target material, which is consistent with the target material of medical X-rays, in order to more conveniently transform the detector to the application scenarios such as medicine. As shown in Fig. 4b, the Ga₂O₃ material displays the following mechanism for X-ray detection: the absorbed X-ray photons excite the bound electrons in the form of collisions, the rest of the energy is converted into electron kinetic energy. X-ray photons impinging on the semiconductor deposit their energy, primarily through the photoelectric effect, exciting electrons from the valence band to the conduction band. This process generates a multitude of electron-hole pairs, these photo-generated carriers are separated by the strong built-in electric field present in the depletion region of the Schottky junction. Under the influence of this field, holes in semiconductors are driven toward the negatively charged side of the depletion layer, while electrons in metals are swept toward the positively charged side. The migration of holes toward the edge of the depletion layer effectively compensates for the fixed negative space charges in that region. This compensation reduces the extent of the space charge region, leading to a narrowing of the depletion layer width. Simultaneously, the accumulation of photo-generated electrons within the semiconductor alters the local electrostatic potential⁴². This accumulation, coupled with the narrowing of the depletion layer, results in a reduction of the built-in potential difference across the junction. Consequently, the energy barrier that governs charge carrier transport—known as the barrier height—is lowered. This integrated mechanism of photo-generated carrier generation and collection, coupled with barrier height modulation, forms the fundamental principle by which this detector converts absorbed X-ray energy into measurable electrical signals.

We adopted a semiconductor analyzer (Keithley, 4200-SCS) to verify the detection performance of the individual element. Supplementary Fig. 6 and Fig. 4c show the I–V curves of this detector element under bipolar and tripolar tests. The dark current curve in Supplementary Fig. 6 represents a typical device, showing that the Schottky junction is formed at the Au/Ga₂O₃ interface. Additionally, <10% deviation in saturated dark current among 32 sampled devices confirmed the pixel homogeneity of our detector (Supplementary Fig. 7). The observed consistency in morphology and I–V behavior strongly suggests reproducible device characteristics—a critical advantage of our printing methodology. Furthermore, the stable, extremely low dark current provides another advantage for this device: an exceptionally low leakage current during non-operating states, ensuring low power consumption. The curve of Fig. 4c characterizes more electrical properties of the detector element. It has an obvious deep valley in the negative voltage region, indicating that the main carriers of the detector element are electrons, while the source-drain current has a significant difference under different gate biases. It is noteworthy that, unlike traditional devices, the current curve in our device shifts to the right as the gate voltage increases. To explain this anomalous phenomenon, we have included the gate current (I_g) measured simultaneously with source-drain current, as shown in Supplementary Fig. 8. Throughout the entire voltage range, the I_g consistently remained at an extremely low level (i.e., within pA range), with no abrupt jumps observed across any order of magnitude. This confirms that the rightward shift in the curve is not attributable to dielectric breakdown. Additionally, we propose the following mechanism to explain this phenomenon: V_{gs} electrostatically dopes the channel, shifting the Fermi level (E_F) relative to the conduction and valence bands. Scanning V_{gs} sweeps E_F from the valence band (hole-dominated transport) through the Charge

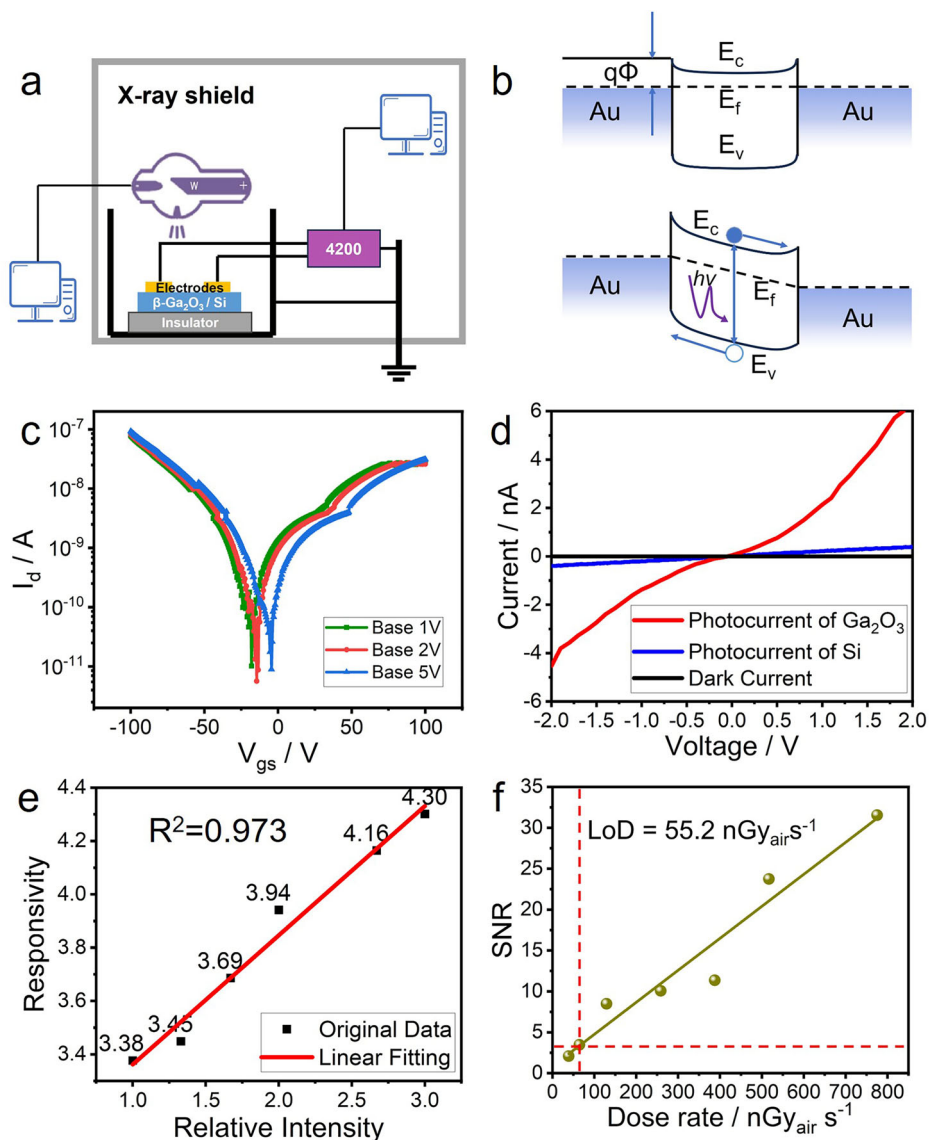
Fig. 3 | Printing of Ga₂O₃-based X-ray detector arrays. **a** Design diagram of the interdigitated electrode, the upper figure shows the detailed parameters of a single interdigitated electrode, and the lower figure shows the layout of the interdigitated electrode array, with the array size of 8 × 8. **b** Flow chart of electrode evaporation, firstly, the mask is fixed on the prepared Ga₂O₃ thin film, and then after fixing it completely, PVD evaporation is carried out, and then after the evaporation is completed, the mask is removed and the electrode array is obtained. **c** Photographs of electrode array, it can be seen that the evaporation electrode layout is very even and clear. **d** Individual electrodes under SEM, under this scale, the electrodes still maintain a very clear contour as well as a homogeneous surface, and the inserted teeth are not distorted and fuzzy, and other defects appear.



Neutrality Point (CNP) (minimum conductance) to the conduction band (electron-dominated transport), creating the characteristic “V” shape. An increasing V_{ds} has two primary effects, it generates a stronger lateral electric field and can induce electrochemical doping or polarization effects at the semiconductor/electrode interface or within the bulk of the material (especially if ionic or polar species are present). The core mechanism is compensatory gate tuning. The electrochemical or polarization effect induced by a higher V_{ds} effectively dopes the channel in a manner equivalent to applying a more positive V_{gs} . This “bias-induced doping” shifts the CNP to a more positive gate voltage. Therefore, to compensate for this V_{ds} -induced shift and return the Fermi level to the CNP (i.e., to find the current minimum again), one must apply a more positive V_{gs} . This is the direct cause of the observed rightward shift. In contrast, in a conventional Field Effect Transistor (FET), a higher V_{ds} simply pulls the channel potential away from the gate’s control, leading to a loss of saturation and an upward shift in the I_d - V_{gs} curve.

This mechanism is not without precedent and has been reported in studies concerning various advanced transistors. A study on GaN FATFETs directly reported that “forward gate bias increased the V_{TH} ” and attributed these “ V_{TH} shifts to electron capturing” at the interface. This is a direct parallel to our observations⁴³. In SiC MOSFETs, research on the dynamic gate stress test of SiC MOSFETs highlights that “threshold voltage drift is the most serious” issue under gate voltage stress. The drift is linked to “interface defects” and “gate oxide charging,” which aligns with our proposed explanation. Furthermore, the degradation of gate electrical parameters in SiC MOSFETs under bias stress also involves threshold voltage drift due to charge trapping in oxide layers⁴⁴. In general FET behavior, the fundamental principle that applying a DC bias to the gate-source junction can set the operating point is well-established. Persistent changes to this bias condition, through mechanisms like charge trapping, can effectively alter the device’s effective threshold, leading to the horizontal shift we observe⁴⁵.

Fig. 4 | Optoelectronic properties of printed Ga₂O₃-based X-ray detector. **a** Schematic diagram for detection system. The Keithley 4200 Source Meter Unit was connected in series to apply bias and simultaneously measure the current generated by the Ga₂O₃ detector. **b** Schematic diagram of electron transition by X-ray motivation. **c** Tri-pole I-V curve of the detector element, using the back side of the wafer as the gate, and a pair of electrodes on the front side as the source and drain, respectively, and the curves shown in this figure are obtained by the test at 1 V, 2 V, and 5 V bias, respectively. **d** Comparison of the detector element's photocurrent with the dark current, it can be seen that in the 20 kV X-ray (radiation dose of 99 $\mu\text{Gy}_{\text{air}}\text{s}^{-1}$) under the light and dark current displays orders of magnitude difference. Besides, it can be seen that the photocurrent of the Ga₂O₃ film exhibits an order-of-magnitude difference compared to that of the silicon wafer at low drive voltages, providing strong evidence that the device's photoconductive response is primarily contributed by gallium oxide. **e** Detection element responsivity curve, in different radiation intensity measurement of light and dark current ratio and take the logarithm, and do the graph linear fitting, get a good linear curve. The number besides the dots shows the logarithm of the current ratio. **f** Device SNR at different dose rates. Based on the image, we determined the device's minimum detection limit (LoD) to be 55.2 nGy/s.



On the other hand, it can be seen that the dark current of the device increases with increasing voltage, probably because the applied bias exacerbates the ion migration inside the device. The detector generates a response current under X-ray irradiation, and the response current density increases with the applied bias voltage, suggesting that the applied electric field also promotes the extraction of photogenerated carriers by the device.

Figure 4d shows the current-voltage (I-V) characteristic curves of a single photodetector cell in the dark state and under X-ray tube irradiation. A back-to-back Schottky junction with an MSM structure is used, where the two contacts are symmetric and the current shows very good symmetry under positive and negative bias voltages. The Schottky barrier height (Φ_B) is determined by the difference between Au work function ($\Phi_M = 5.1$ eV) and Ga₂O₃ electron affinity ($\chi = 4.0$ eV), following $\Phi_B = \Phi_M - \chi$ (Schottky–Mott rule). Amorphous Ga₂O₃ films prepared in an O₂ containing atmosphere can suppress the defect states of the films and reduce the carrier concentration, and the dark current of the obtained devices can be maintained at a low level. From the figure, it can be seen that the dark current of the device is extremely low, only 0.01 nA at 10 V bias, which is mainly due to the high resistivity and wide forbidden bandwidth of the prepared Ga₂O₃. Low dark current is one of the basic requirements for realizing high signal-to-noise ratio X-ray detectors. When there is X-ray illumination, the photocurrent of the device is obviously larger than the dark

current, and there is an increase of several orders of magnitude. As supplementary Fig. 9 shows, at 10 V bias voltage and the dose rate of $1.55 \mu\text{Gy}\text{s}^{-1}$, the photocurrent is about 1.5 nA, which is two orders of magnitude larger than the corresponding dark current, which indicates that the prepared device has good photosensitive characteristics and has great potential for application in X-ray detection. Simultaneously, to rule out any potential influence of the silicon substrate on X-ray response, we compared the photocurrent of the silicon wafer under identical conditions with that of our detector device. Figure 4d demonstrates that its photocurrent is one order of magnitude lower than that of the detector device, confirming that the silicon substrate has a negligible impact on detector performance.

Additionally, to verify the detector's reliability, we tested its photocurrent response under different radiation dose rates (Supplementary Fig. 10). The figure shows that under specific bias, the device's photocurrent exhibits a clear positive correlation with dose rate. Simultaneously, each photocurrent curve in the figure displays the classic MSM structural characteristics. Together, these phenomena demonstrate that the device possesses excellent X-ray detection performance. Furthermore, to more precisely quantify the X-ray detection performance of the device, we tested the responsivity of the X-ray detector under X-ray irradiation of different dose rate, showing the result in Fig. 4e. The responsivity of the detector was calibrated using a relative intensity scale referenced to a defined baseline

X-ray flux. The baseline flux was established at a tube voltage of 20 kV and a tube current of 300 μA , corresponding to a measured air kerma rate of 49.5 $\mu\text{Gy/s}$. This baseline condition was assigned a relative intensity of 1. The X-ray tube current was then systematically varied from 300 μA to 900 μA (at constant 20 kV), thereby proportionally increasing the relative intensity (and the air kerma rate). For each tube current setting, the photocurrent (I_{light}) under X-ray exposure and the dark current (I_{dark}) were measured. Since we observed that the photocurrent does not follow a linear relationship with the dose rate in the detectors reported in this paper, according to the conventional definition of responsivity, responsivity varies significantly at different dose rates, which may lead to confusion regarding the device's response performance. Therefore, we adopted a new definition, namely Logarithmic Responsivity that differs from conventional methods, to characterize the photo-response properties of this device. The detector's logarithmic responsivity (R) was then calculated using the formula:

$$R = \log_{10} \left(\frac{I_{\text{light}}}{I_{\text{dark}}} \right) \quad (1)$$

Finally, the calculated R values were plotted as a function of the relative intensity and fitted with a linear function to characterize the detector's response linearity over the tested flux range. From the figure, it can be seen that the device in any ray intensity, have a good optical response, and the logarithmic responsivity and ray intensity into an obvious linear relationship, the fit to get $R^2 = 0.973$, which fully demonstrates that the detector can be different intensity of X-rays of different intensity of the optical response, with a good intensity resolution. Unlike most photodetectors, our device exhibits a pronounced superlinear increase in photocurrent with dose rate within the tested range. After comparing various fitting methods, the exponential law most closely approximates this superlinear growth. Regarding this phenomenon, we proposed a different regime: At low dose rates, a large number of deep-level traps in the material (such as oxygen vacancies) capture photo-generated carriers. These trapped charges cannot participate in conduction and form space charges within the detector that create counter-electric fields, resulting in extremely low carrier collection efficiency and minimal photocurrent. As the dose rate increases, the number of generated carriers grows, beginning to fill these traps⁴⁶. As traps gradually fill, two critical changes occur: reduced trap-assisted recombination and enhanced built-in electric field. The decrease in trap-assisted recombination significantly increases carrier lifetime, while the enhanced built-in electric field—formed by trapped hole charges—reinforces the applied electric field. This combination dramatically boosts carrier collection efficiency (the μt product). Together, these form a positive feedback loop, more carriers enable more traps to be filled, achieving higher collection efficiency, ultimately deploying more carriers. This manifests in the curve as a segment where the photocurrent exhibits superlinear or even near-exponential growth with dose rate.

The detector demonstrates exceptional stability and consistency across a wide range of dose rates, confirming its robustness for practical applications in dynamic radiation environments. This further underscores its potential for accurate and reliable dose measurements without requiring complex calibration procedures. Such performance advantages highlight the detector's suitability for real-time radiation monitoring systems where precision and reliability are paramount. Furthermore, the response levels at different dose rates derived from the fitted straight lines also align with the results presented in the Supplementary Fig. 10. It should be noted that Intrinsic material resolution \neq electrode sampling limit, the 20 nm quasi-2D Ga_2O_3 film confines charge carriers laterally within <200 nm (by $>10^9 \Omega\text{-cm}$ resistivity), enabling material-limited resolution of 1.2 μm . This is governed by carrier diffusion length ($L = \sqrt{D\tau} < 0.2 \mu\text{m}$)⁴⁷, not electrode pitch. Electrode spacing sets the Nyquist sampling limit (750 μm), but does not degrade the intrinsic resolution, as demonstrated in thin-film detectors where sub- μm resolution persists at mm-scale pitches⁴⁸. In addition, the claimed 1.2 μm resolution refers to the detector's intrinsic capability (validated by charge-collection efficiency models). The imaging system's

Table 1 | Comparison of the performance between the X-ray detectors in this work and the detectors reported in the literature

Material	Thickness (nm)	Driving voltage (V)	Sensitivity ($\mu\text{C Gy}^{-1} \text{cm}^{-2}$)
$\text{CH}_3\text{NH}_3\text{PbI}_3$ ³	600	0	1.5 (calculated by bulk sensitivity)
amorphous Ga_2O_3 ⁵⁹	250	50	6.77 (calculated by bulk sensitivity)
IGZO ⁶⁰	300	0.3	8.5
Pentacene ⁶¹	300	−4	4.87 (calculated by bulk sensitivity)
$\kappa\text{-Ga}_2\text{O}_3$ ²⁸	440	500	15
GaN ²	5.7×10^3	0	0.17
CsPbBr_3 ⁵⁴	20	0.1	1450
$\beta\text{-Ga}_2\text{O}_3/\text{Mg}$ ⁶²	10^6	−1000	338.9
$\text{Cs}_2\text{AgBiBr}_6$ ⁶³	10^5	400	40
Diamond ⁶⁴	3×10^5	300	44.46 (calculated by bulk sensitivity)
Quantum Dots ⁶⁵	2×10^3	1	431
Perovskites ⁶⁶	6×10^3	1	1409
Ga_2O_3 (this work)	30	−10	6050

effective resolution (15 μm) is dominated by optics/scintillator limitations, consistent with Siemens star results (5.6 lp/mm \approx 178 μm). Large spacing prevents electrical crosstalk while preserving signal fidelity—a trade-off also adopted in diamond detectors⁴⁹. Therefore, it proves that the detector array has a good imaging detection basis in theory.

Assuming almost no energy loss during transmission, the local irradiation dose rate of the device can be calculated using the following expression⁵⁰

$$D = D_{\text{tot}} \times \frac{A}{A_{\text{tot}}} \quad (2)$$

where D_{tot} is the total dose rate of the entire X-ray irradiated area, A_{tot} is the area of the total irradiated area, and D and A are the dose rate and effective area of each device. Considering that the total dose rate D_{tot} of X-rays at 20 kV 600 μA is 99 μGys^{-1} , the total effective irradiated area A_{tot} is about 1024 mm^2 , and the effective area A of a single device is 16 mm^2 . According to the formula, we can obtain that the dose rate of a single device will be about 1.55 μGys^{-1} . Under this dose rate, the average response current of X-rays is about 1.5 nA under the bias of 10 V. Therefore, one has:

$$S = \frac{\Delta I}{A \times D} \quad (3)$$

where S is the sensitivity and I is the response current to X-rays, the sensitivity is calculated to be 6050 $\mu\text{C/Gy/cm}^2$. Notably, since the photocurrent of this device does not exhibit a linear relationship with the dose rate, the sensitivity defined by Eq. (3) also varies with changes in dose rate. To facilitate comparison with other X-ray detectors, we set the sensitivity at 1.55 μGys^{-1} as the reference point. After obtaining the sensitivity of the Ga_2O_3 thin film, we made a side-by-side comparison with the existing thin film X-ray detectors, focusing on the three parameters of sensitivity, driving voltage, and thickness, as shown in Table 1. The comparison results show that the thin-film detector in this work has the advantages of high sensitivity and low driving voltage, and the performance has a great advantage over the remaining gallium-based thin-film devices. It can be seen that the sensitivity of our prepared devices occupies a clear advantage, coupled with the characteristics of the film preparation process is simple, easy to repeat and

large area preparation, which is of great significance for X-ray detection of materials. The sensitivity of our detectors far exceeds that of conventional α -Se detectors ($20 \mu\text{C}/\text{Gy}/\text{cm}^2$).

We adopt the simplified model used by Girolami et al.⁵¹, according to which the theoretical upper limit of the surface sensitivity (S_{max}) is given by:

$$S_{\text{max}} = \frac{e\mu_p\rho d}{\mu E_i} \quad (4)$$

$$E_i = 2E_g + 1.43 \quad (5)$$

where $e = 1.61 \times 10^{-19} \text{ C}$ is the electron charge, μ_p and μ ($\text{cm}^2 \text{ g}^{-1}$) are the mass attenuation coefficients of the active layer material and dry air, respectively, at the photon energy E_{ph} . In the case of the device introduced in this work, the active material is a Ga_2O_3 thin film with thickness $d = 3 \times 10^{-8} \text{ m}$. We can now obtain simple operative expression to evaluate S_{max} . We assumed the density of Ga_2O_3 $\rho = 5.9 \text{ g cm}^{-3}$, by considering a photon energy $E_{\text{ph}} = 20 \text{ keV}$, which is the most probable energy in the case of a W-target X-ray tube, the mass attenuation coefficient⁵² is $\mu_p = 29.44 \text{ cm}^2 \text{ g}^{-1}$. At the same photon energy (20 keV), the mass attenuation coefficient of dry air is $\mu = 9.92 \text{ cm}^2 \text{ g}^{-1}$. Finally, being the bandgap energy $E_g = 4.26 \text{ eV}$, the estimated electron-hole pair creation energy is $E_i = 2 \cdot 4.26 + 1.43 = 9.95 \text{ eV} = 1.594 \times 10^{-18} \text{ J}$. The calculation yields $S_{\text{max}} \approx 53.056 \mu\text{C Gy}^{-1} \text{ cm}^{-2}$, which is much lower than the measured value ($6050 \mu\text{C Gy}^{-1} \text{ cm}^{-2}$), thus confirming the existence of photoconductive gain. And the gain $G = S/S_{\text{max}} = 114$ shows typical gain value of 2D devices.

For X-ray detectors, the minimum detection limit (LoD) is an important parameter. We measured the device's SNR at dose rates of 39, 64, 130, 260, 387, 520, and 775 nGy/s, obtaining a curve of SNR versus dose rate, and the curve is shown in Fig. 4f. Following standard practice, we define the dose rate corresponding to SNR = 3 as the minimum detection limit for this detector. Based on the image analysis, we calculated the minimum detection limit for this detector to be 55.2 nGy/s. This value demonstrates extraordinary detection performance for X-ray and meets medical testing requirements ($5.5 \mu\text{Gy}_{\text{air}}/\text{s}$)⁴.

Since our films own homogeneity and support multi-channel detection on surface arrays, we have innovatively applied gallium-based semiconductor films to X-ray imaging, thus creating a low-cost, large-area, high-performance X-ray imaging system, the schematic of the system is shown in Fig. 5a. X-ray imaging systems are able to utilize the advantages of multiple devices to obtain high contrast images with a small irradiation dose. In order to effectively prevent the problem of current crosstalk from multiple devices, each detector needs to be discrete and does not interfere with each other during testing. While this proof-of-concept array has a limited field of view, the quasi-2D nature and semiconductor compatibility of the Ga_2O_3 film make it highly suitable for integration into the miniaturized and modular imaging systems that represent the future of diagnostic and non-destructive testing technology. To verify the long-term stability of this detector, we stored a sample under natural conditions for 1 year and irradiated it with an identical dose rate during testing. This yielded a comparison of the photocurrent between the fresh sample and the sample after 1 year, as shown in Fig. 5b. According to the test data, the device exhibited less than 15% performance degradation after 1 year, demonstrating excellent long-term stability. Furthermore, we measured its response time. The change in current of the device over the time was measured by periodically switching the X-rays on and off, i.e., time-dependent photo-response performance testing. The results in Fig. 5c show that the device exhibits reproducible time-dependent response properties with cyclic X-ray irradiation both at a constant voltage bias of 10 V and after six cycles of switching the light on and off. Figure 5c clearly shows six distinct ON and OFF periods. Following standard procedures, we selected six complete periodic signals that had reached steady-state signal arrival for measurement⁵³. The responses are highly consistent but not artificially identical, displaying the minor fluctuations characteristic of experimental data. As it can be seen in Supplementary

Fig. 11, the rising (from 10% to 90% of the saturated X-ray signal) and falling (from 90% to 10% of the saturated X-ray signal) times of the detector based on Ga_2O_3 film under 10 V bias are about 43.7 and 42.6 ms, respectively, showing a relatively fast response time. The periodic repeatability shown in Fig. 5c and the intra-cycle stability presented in Supplementary Fig. 11 collectively demonstrate that the device exhibits excellent cycling stability. During testing the Ga_2O_3 devices consistently maintained a stable low response current and sensitive response speed during X-ray irradiation, and the dark current was consistently maintained on the order of pico-ampere. This remarkable combination of ultralow dark current and rapid response highlights the detector's excellent signal-to-noise ratio and operational stability in radiation detection. Such performance not only ensures accurate signal acquisition under low-dose exposures but also underscores the potential of Ga_2O_3 -based detectors for use in high-precision radiography and low-dose diagnostic applications, offering a significant advantage over conventional detectors that often suffer from high noise and slow response times.

Furthermore, we explored the rising edge and falling edge response times in several cycles, and counted them and drew box line plots and normal curves, showing the results in Fig. 5d. The Q1, Q2 and Q3 bins of the statistics are presented in the figure, and the extreme deviation of each set of data is labeled with error bar. The figure shows that the rising edge response time has a relative standard error of 5% while the falling edge has a relative standard error of 7%, verifying the stability of the detector response time. In CT imaging, the X-ray exposure time per tomographic scan correlates with the source rotation speed. Conventional CT imaging operates at a sampling frame rate of 30 Hz, requiring device response times not exceeding 50 ms (Nyquist sampling limit). The X-ray detector response time in this study meets the aforementioned requirements, and Fig. 5d shows the excellent stability of the detector response time, thereby demonstrating its potential application value in medical CT scanning.

Supplementary Fig. 12 shows the schematic diagram of the imaging test system we built, the imaging test is carried out in a ray-shielded environment, and the copper sheet with a thickness of 1 mm is cut into the shape of "L" and "M", and fixed in the position of 4 mm above the array through the hollow bracket, in order to avoid metal-to-metal contact leading to short circuits and other unexpected phenomena. During imaging tests, we placed different imaging objects such as the letters "L" and "M" in front of the photodetector array to produce different light fields on the photodetector array plane. During the imaging process, we manually selected the pixels to be tested one by one, and the signal acquisition device—semiconductor analyzer—collected the current output signals from each photodetector unit. Subsequently, using Matlab software, we combined the photodetector's output current with the corresponding position coordinates to reconstruct the image. Figure 5e shows the imaging objects and their corresponding imaging results. As can be seen, these images can be clearly identified, indicating that quasi-2D Ga_2O_3 -based X-ray photodetector arrays have potential application prospects in CT imaging. Figure 5e is the spatial distribution of the X-ray intensity measured after we used a copper sheet to block the X-rays, and it can be seen that the detector clearly presents the "L" "M" At the same time, we look at the part that is not covered by the copper sheet, and its logarithm responsivity is very uniform, and there is no noise, bad spots and other phenomena. On the other hand, there is a significant decrease in the logarithm responsivity of the part obscured by the copper sheet, and according to the data of the fitted straight line, the X-ray intensity is calculated to be 0.45 times of the relative intensity, which is similar to the result obtained from the calculation of the linear absorption coefficient of X-rays of the copper sheet. Further, it can be seen from the figure that there is a slight decrease in logarithm responsivity at the outer edge of the part shaded by the copper sheet, which should be attributed to the existence of a slight shielding of the outer edge portion of the array by the copper sheet, which does not shield the main part of the electrodes but affects the total radiation intensity of the electrode region at the outer edge, producing a slight decrease. While large electrode spacing reduces sampling density, it enables high-voltage operation (>100 V) without breakdown. The 15 μm

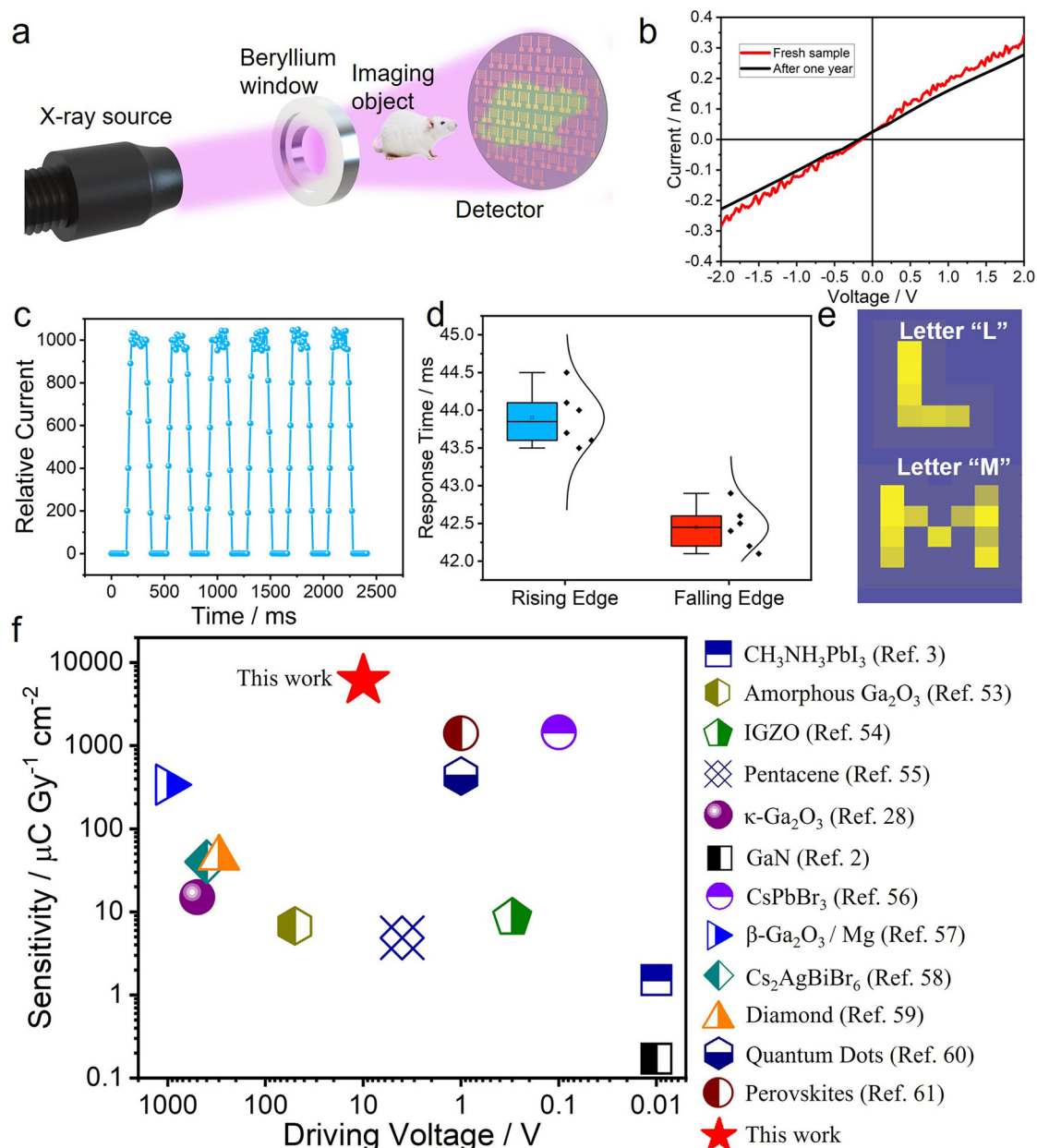


Fig. 5 | X-ray imaging output of Ga₂O₃ detectors. **a** Schematic diagram of X-ray imaging. The field of view in this direct-irradiation configuration is constrained by the physical area of the 8×8 array (approximately 3.2 × 3.2 cm²), limiting the object size for a single-shot image. Future systems could incorporate optical focusing elements or scanning mechanisms to image larger objects. The animal on the schematic represents any object. **b** Comparison of photocurrent between fresh samples and the same samples after one year. Samples stored under ambient conditions for one year exhibited photocurrent responses close to those of fresh samples, demonstrating the device’s excellent long-term stability. **c** Response time test of the detector, were measured six cycles, with the average response time of the rising edge as 43.8 ms, while the falling edge response time as 42.5 ms, at the same time. The

relative current of the illumination is around 1000, which shows that it owns the characteristics of cyclic stability. **d** Box plots of the rising and falling edge response times of the detector, with the boxes indicating the Q1 through Q3 bins, the error bar reflecting the extreme deviation of each set of data, and the normal curve showing the distribution of response times. **e** Imaging validation effect diagram of the detector, using 1 mm thickness of copper shielding X-rays, and measure its relative current, high relative current is marked in blue, low relative current is marked in yellow. The imaging of the “L” and “M” letters are clearly seen. Further, the corner and the structure are clearly displayed. **f** Comparison of detector performance, our work is marked as a red pentagram in the figure.

system resolution remains suitable for medical/industrial applications (e.g., mammography requires 5–10 lp/mm). Future designs may implement multi-scale electrodes to bypass this trade-off.

After verifying the X-ray detection performance, we made a side-by-side comparison of the present work with previously reported X-ray detectors, focusing on two metrics, sensitivity and drive voltage, and the results are shown in Fig. 5f. Our detectors feature top-tier sensitivity while

operating at a low driving voltage (10 V). While several recent reports on optimized thin-film sensors have demonstrated high sensitivity in the order of 10³ μC/Gy/cm² at operating voltages below 5 V^{54,55}, our work distinguishes itself through a different set of advantages in simplified fabrication process and enhanced stability. Solution-printed quasi-2D Ga₂O₃ detectors combine industry-compatible fabrication, peer-leading sensitivity and record-low operating voltage (10 V)—critical for monolithic integration

with back-end-of-line integration⁵⁶, ensures that our detector can function in electronic circuit chips without contaminating the silicon substrate⁵⁷, demonstrating that our technology fills a critical niche in low-voltage, printable detectors for integrated imaging systems. Admittedly, the 10 V driving voltage limits its ability to integrate directly with CMOS circuits. However, its relatively low voltage preserves the potential for implementing system-level solutions using interface circuits⁵⁸.

Conclusion

In summary, we demonstrate a novel low-cost printing process for quasi-2D Ga₂O₃ and X-ray detectors. This straightforward and efficient method enables rapid large-area fabrication of quasi-2D Ga₂O₃ with uniform film quality and thickness control, providing a critical foundation for achieving high spatial resolution in pixelated arrays. Simultaneously, the wide bandgap (~4.26 eV) and low dark current of quasi-2D Ga₂O₃ inherently favor potential-resolution detection by suppressing noise sources that degrade energy resolution in narrow-gap materials. Meanwhile, the wide bandgap (~4 eV) and low dark current of quasi-2D Ga₂O₃ create inherent advantages for potential energy-resolved detection by suppressing noise sources that degrade energy discrimination in narrow-gap materials. We systematically study the detection performance of the detector, showing good spatial resolution and energy resolution, large differences in the responsivity to different intensities of X-rays (slope), and the logarithm responsivity and the X-ray intensity with a good linear relationship (R-squared), in terms of spatial resolution, the tiny detector element (element linearity) to ensure that the device can be in the mm precision detection of the intensity distribution of spatial X-rays. The device exhibits a falling-edge response time of less than 45 ms, which proves that the device has a good transient response to X-rays, and this also lays a solid foundation for new CT imaging. We have also constructed an 8 × 8 X-ray detection imaging array system based on amorphous quasi-2D Ga₂O₃ using liquid metal nanoimprinting technology for the first time. This work provides a simple, efficient and low-cost new strategy for large-area, high-quality and controllable preparation of next-generation high-performance X-ray detectors and imaging systems, which is of great significance and value for the development of sensitive, fast and stable X-ray imaging detectors and even CT core detection components. While this study focuses on foundational sensitivity and low-voltage operation metrics, quantitative spatial/energy resolution measurements require pixelated array integration and spectroscopic characterization—important next steps for practical implementation.

Methods

Film growth and device preparation

The film is grown on P-type single-throw 4-inch wafers (100 crystal faces, oxide layer thickness of 5000 Å). In order to ensure good contact between the Ga₂O₃ film and the wafer when printing, the plasma cleaner of Tangshan Yanzhao Science and Technology Research Institute, model YZD08-2C, is used to carry out ultraviolet bonding treatment, treatment time 2 min, oxygen flow rate of 0.6 L/min. After plasma treatment, the sample is fixed with high-temperature tape on an adjustable-temperature heating table of Chint Electric Model NXB-63 and heated to 150 °C and started liquid metal printing. Eutectic gallium indium (EGaIn) was made from Ga (4N purity, China New Metal Materials Technology Co., Ltd) and In (99.995% purity, Zhuzhou Konen New Materials Co., Ltd) with a mass ratio of 75.5:24.5, and was also heated to 150 °C, and flexible PDMS sheets were used to print the EGaIn liquid onto the wafer. EGaIn liquid was coated and printed on the wafer using a flexible PDMS sheet, and each printing process lasted for 3 min, after which the EGaIn droplets were recovered, and the residual liquid metal on the wafer surface was wiped with boiling anhydrous ethanol, and the above process was repeated for 10 times after wiping to obtain Ga₂O₃ films with very good homogeneity. After that, gold electrode is vaporized on the film by the PVD method, using a vaporizer of Changzhou Hongming Instrument HM-ETD-2000C, with 0.15 mbar of argon in the chamber for 5 min, and the current was kept at 20 mA to vaporize a uniform layer of gold electrode.

Surface characterization and composition verification

Metallurgical microscope model LV-UEPI-N from Nikon, Japan, is used firstly to observe the macroscopic homogeneity of the samples at a magnification scale of 200 times. After that, the surface flatness was examined using a Bruker FastScan atomic force microscope with a scanning range of 50 μm × 50 μm. To verify the film composition, XPS test (ESCALAB250Xi, by ThermoFisher Scientific, China) was used to detect the X-ray photoelectrons of Ga 2p, Ga 3d, and O 1s orbitals in the energy intervals of 1110–1145 eV, 14–30 eV, and 525–545 eV, which can be verified that the films contain only Ga₂O₃ by comparing with the results of the EDS analysis (QUANTA FEG 250, FEI, US). Optical band gaps were calculated via absorption of the films, which were measured through UV-VIS-NIR spectrophotometer (Cary 7000, Agilent, US). Moreover, to show the shape of the electrodes, SEM (QUANTA FEG 250, FEI, US) was used with a scanning range of 2 mm × 2 mm.

Electrical performance testing

The electrical performance tests covered in this paper were performed using a high-precision Lake Shore's 4200 parameter analyzer. The Ga₂O₃ film contact test was conducted by I-V test, with the voltage scanned from -10 to 10 V in 0.1 V. In the carrier characterization test, the wafer is polished and sprayed gold on the backside as the gate, and applied bias voltages of 1 V, 2 V, and 5 V, which were all scanned from -50 to 50 V in 0.5 V increments.

For the photodetection part, X-ray tube from Dandong Shenbo Electronic Instruments (Tungsten Target) is used, with an applied tube voltage of 20 kV, a tube current of 600 μA, and a beryllium window of 5 cm from the sample, and the above parameters were also applied to the X-ray tube parameters for imaging detection and to those for response time. While for the responsivity test, the tube voltage is kept constant and the tube current is changed from 300 to 900 μA to measure its photocurrent, respectively. Additionally, the incident dose rate in air at the surface of the detector was calculated based on the pre-calibrated output of the X-ray source, determined using a HA1100Med calibrated ion chamber and electrometer. The dose rate was varied by adjusting the tube current (I) while keeping the tube voltage (V) constant at 20 kV.

For the response time test, the ray tube parameters were chosen as mentioned before, i.e., tube voltage of 20 kV, tube current of 600 μA, and its ray intensity of 99 μGys⁻¹. The response time was determined through direct optical switching measurements with pulse generators (Teslaman TXMP1006, Dalian, China). Each pulse lasts 200 ms, with a 200 ms interval between pulses to ensure complete system stabilization, which ensures that the device has sufficient time to relax back to the ground state when there is no ray irradiation. Current transients were recorded at 10 Hz sampling (Keithley 4200-SCS, integration time 10 ms). The 43.8 ms rise time represents the 10–90% transition duration averaged over 6 shutter cycles, while the Keithley 4200-SCS parameter analyzer recorded the photocurrent temporal response at 10 ms sampling intervals (integration time per data point).

Image reproduction

In this work, the detection arrays are laid out in 8 × 8 squares, so the images are also divided into 8 × 8 square arrays during image reproduction, and the color of each small square represents the logarithm of the light-to-dark current ratio, i.e., the logarithm responsivity, with blue representing a high logarithm responsivity and yellow representing a low logarithm responsivity.

The 64 sensors (8 × 8 matrix) were fabricated on a common substrate with a shared ground electrode. Each pixel's top electrode was connected to an individual readout channel via low-noise, shielded coaxial cables. A single, stable DC bias of 10 V was applied to the common ground plane, biasing all pixels simultaneously and uniformly. We employed two National Instruments PXIe-4302 high-density analog input modules (32 channels each, 64 total) installed in a PXIe-1082 chassis controlled by a PXIe-8880 controller. This system allows for perfectly simultaneous, synchronous sampling across all 64 channels. All channels share a common analog-to-

digital converter clock and trigger, eliminating timing skew between pixel measurements. For the imaging experiment, data was acquired at a rate of 1 Hz (1 sample per second per channel). This rate was chosen as it adequately captures the slow variation in X-ray exposure during the imaging process while maximizing the signal-to-noise ratio. The raw current data from all 64 channels was streamed directly to a PC running LabVIEW software. The software displayed the real-time current values for monitoring. For image construction, the average photocurrent ($I_{\text{photo}} - I_{\text{dark}}$) for each pixel over a stable exposure period was calculated. This 8×8 matrix of values was then mapped to a grayscale image using MATLAB, as shown in Fig. 5e.

Data availability

The data used to determine the data points shown within the plots presented in this paper, and other findings from this study, are available from the corresponding author Jing Liu upon reasonable request. The email address of Jing Liu is: jlui@mail.ipc.ac.cn.

Received: 24 June 2025; Accepted: 16 December 2025;

Published online: 29 December 2025

References

- Rowlands, J. A. Material change for X-ray detectors. *Nature* **550**, 47–48 (2017).
- Zhou, L. et al. Self-powered fast-response X-ray detectors based on vertical GaN p-n diodes. *IEEE Electron Device Lett.* **40**, 1044–1047 (2019).
- Yakunin, S. et al. Detection of X-ray photons by solution-processed lead halide perovskites. *Nat. Photonics* **9**, 444–449 (2015).
- Wei, H. et al. Sensitive X-ray detectors made of methylammonium lead tribromide perovskite single crystals. *Nat. Photonics* **10**, 333–339 (2016).
- Sabottke, C. F. & Spieler, B. M. The effect of image resolution on deep learning in radiography. *Radiology* **2**, e190015 (2020).
- Moy, J.-P. Recent developments in X-ray imaging detectors. *Nucl. Instrum. Methods Phys. Res. Sect. A* **442**, 26–37 (2000).
- Chotas, H. G., Dobbins, J. T. & Ravin, C. E. Principles of digital radiography with large-area, electronically readable detectors: a review of the basics. *Radiology* **210**, 595–599 (1999).
- Holland, S. E., Wang, N. W. & Moses, W. W. Development of low noise, back-side illuminated silicon photodiode arrays. *IEEE Trans. Nucl. Sci.* **44**, 443–447 (1997).
- Song, S.-Y. et al. Scalable X-ray scintillators with bright singlet-triplet hybrid self-trapping excitons. *Light Sci. Appl.* **14**, 249 (2025).
- Yang, Z. et al. Na-alloy tailored 3D/0D metal halide heterostructures enabling efficient charge transfer for color-integrated white scintillators. *Nat. Commun.* **16**, 6909 (2025).
- Deng, Y. et al. Manganese halide-based glass-ceramic scintillator for ultra-stable and multi-functional x-ray imaging in extreme environments. *Laser Photon. Rev.* e011178 <https://doi.org/10.1002/lpor.202501178>.
- Mescher, H. et al. Flexible inkjet-printed triple cation perovskite X-ray detectors. *ACS Appl. Mater. Interfaces* **12**, 15774–15784 (2020).
- Zhang, C. et al. X-ray detectors based on Ga₂O₃ microwires. *Materials* **16**, 4742 (2023).
- Wang, B. et al. One-dimensional CsCu₂I₃ single-crystal X-ray detectors. *ACS Energy Lett.* **8**, 4406–4413 (2023).
- Belev, G. & Kasap, S. O. Amorphous selenium as an X-ray photoconductor. *J. Non-Crystalline Solids* **345–346**, 484–488 (2004).
- Swierkowski, S. P., Armantrout, G. A. & Wichner, R. Recent advances with HgI₂ X-Ray detectors. *IEEE Trans. Nucl. Sci.* **21**, 302–304 (1974).
- Sun, H. et al. Electrical behavior of X-ray detector based on PbI₂ crystal with coplanar electrode structure. *IEEE Trans. Nucl. Sci.* **63**, 1790–1796 (2016).
- Roy, U. N. et al. Al-doped ZnO contact to CdZnTe for x- and gamma-ray detector applications. *Appl. Phys. Lett.* **108**, 242106 (2016).
- Qamar, A. et al. X-ray spectroscopic study of amorphous and polycrystalline PbO films, α-PbO, and β-PbO for direct conversion imaging. *Sci. Rep.* **7**, 13159 (2017).
- Pan, W. et al. Cs₂AgBiBr₆ single-crystal X-ray detectors with a low detection limit. *Nat. Photonics* **11**, 726–732 (2017).
- Nanayakkara, M. P. A. et al. Tissue equivalent curved organic X-ray detectors utilizing high atomic number polythiophene analogues. *Adv. Sci.* **10**, 2304261 (2023).
- Looker, Q. et al. Synchrotron characterization of high-Z, current-mode x-ray detectors. *Rev. Sci. Instrum.* **91**, 023509 (2020).
- Song, Z. et al. Quantitative modeling of perovskite-based direct X-ray flat panel detectors. *Front. Optoelectron.* **17**, 32 (2024).
- Starkholm, A. et al. Green fabrication of sulfonium-containing bismuth materials for high-sensitivity X-ray detection. *Adv. Mater.* **37**, 2418626 (2025).
- Jones, D. C., Jollands, M. C., D'Haenens-Johansson, U. F. S., Muchnikov, A. B. & Tsai, T.-H. Development of a large volume line scanning, high spectral range and resolution 3D hyperspectral photoluminescence imaging microscope for diamond and other high refractive index materials. *Opt. Express* **32**, 15231–15242 (2024).
- Xu, P., Yu, Y., Zhou, H. & Qiu, C. A large-grain-size thick-film polycrystalline diamond detector for X-ray detection. *Plasma Sci. Technol.* **22**, 125601 (2020).
- Shao, H. et al. Amorphous Ga₂O₃ semiconductor: a new solution for robust X-Ray dosimeters. *Adv. Funct. Mater.* **35**, 2421730 (2025).
- Girolami, M. et al. Orthorhombic undoped κ-Ga₂O₃ epitaxial thin films for sensitive, fast, and stable direct X-ray detectors. *J. Mater. Chem. C* **11**, 3759–3769 (2023).
- Mykhaylyk, V. B., Kraus, H., Kapustianyk, V. & Rudko, M. Low temperature scintillation properties of Ga₂O₃. *Appl. Phys. Lett.* **115**, 081103 (2019).
- Venkata Prasad, C. et al. Ga₂O₃-based X-ray detector and scintillators: a review. *Mater. Today Phys.* **35**, 101095 (2023).
- Liu, Y. et al. Reservoir computing based on oxygen-vacancy-mediated X-ray optical synaptic device for medical CT bone diagnosis. *ACS Appl. Mater. Interfaces* **16**, 24871–24878 (2024).
- Ouyang, X. et al. Performance degradation of Ga₂O₃-based X-ray detector under gamma-ray irradiation. *Micromachines* **16**, 339 (2025).
- Chen, Y. et al. Flexible single microwire X-ray detector with ultrahigh sensitivity for portable radiation detection system. *Adv. Mater.* **36**, 2404656 (2024).
- Prasad, C. V. et al. Fast-response, self-powered staggered-gap p-CuGaO₂/β-Ga₂O₃ heterojunction for large-area diagnostic X-ray imaging applications. *Sens. Actuators A Phys.* **383**, 116243 (2025).
- Zavabeti, A. et al. A liquid metal reaction environment for the room-temperature synthesis of atomically thin metal oxides. *Science* **358**, 332–335 (2017).
- Cabrera, N. & Mott, N. F. Theory of the oxidation of metals. *Rep. Prog. Phys.* **12**, 163 (1949).
- Zheng, Y.-T. et al. Effect of anisotropic electron transfer on the reactive nucleation of oxide nanowires. *Chem. Phys. Lett.* **750**, 137505 (2020).
- Zheng, Y.-T. et al. Effect of ionization on the oxidation kinetics of aluminum nanoparticles. *Chem. Phys. Lett.* **696**, 8–11 (2018).
- Janotti, A. et al. Hybrid functional studies of the oxygen vacancy in TiO₂. *Phys. Rev. B* **81**, 085212 (2010).
- Chen, Y. et al. Bandgap engineering of Gallium oxides by crystalline disorder. *Mater. Today Phys.* **18**, 100369 (2021).
- Rajapitamahuni, A. K. et al. Plasmon–phonon coupling in electrostatically gated β-Ga₂O₃ films with mobility exceeding 200 cm² V⁻¹ s⁻¹. *ACS Nano* **16**, 8812–8819 (2022).
- Zeng, X. et al. Achieving effective self-driven X-ray detection sensitivity via pyroelectric–photovoltaic coupling in a layered perovskite pyroelectric. *ACS Energy Lett.* **9**, 381–387 (2024).

43. Irokawa, Y. et al. Gate-bias-induced threshold voltage shifts in GaN FATFETs. *ECS J. Solid State Sci. Technol.* **12**, 055007 (2023).
44. Tang, L. et al. Analyzing the changes in the third quadrant characteristics of SiC MOSFET induced by threshold drift. *IEEE Trans. Electron Devices* **71**, 2342–2348 (2024).
45. Lee, T. Y., Kim, Y. J., Ahn, S. & Jeon, D. Y. Electrically tunable ideality factor and series resistance of gate-controlled graphene/pentacene Schottky junctions. *IEEE J. Electron Devices Soc.* **12**, 379–383 (2024).
46. Mcglone, J. F. et al. Trapping effects in Si δ -doped β -Ga₂O₃ MESFETs on an Fe-doped β -Ga₂O₃ substrate. *IEEE Electron Device Lett.* **39**, 1042–1045 (2018).
47. Ritter, D., Weiser, K. & Zeldov, E. Steady-state photocarrier grating technique for diffusion-length measurement in semiconductors: theory and experimental results for amorphous silicon and semi-insulating GaAs. *J. Appl. Phys.* **62**, 4563–4570 (1987).
48. Konstantinidis, A. C. et al. X-ray performance evaluation of the Dexela CMOS APS X-ray detector using monochromatic synchrotron radiation in the mammographic energy range. *IEEE Trans. Nucl. Sci.* **60**, 3969–3980 (2013).
49. Xue, J. et al. Silicon substrate diamond film detector for gamma dose rate measurement in a high radiation environment. *Diam. Relat. Mater.* **121**, 108752 (2022).
50. Lu, Z., Kang, H., Zhong, Z. & Zhang, T. Structural, electrical and optical properties of transparent conductive titanium–gallium–zinc oxide films by magnetron sputtering. *J. Mater. Sci.: Mater. Electron.* **27**, 13271–13279 (2016).
51. Girolami, M. et al. Metal-halide perovskite submicrometer-thick films for ultra-stable self-powered direct X-ray detectors. *Nano-Micro Lett.* **16**, 182 (2024).
52. Devanathan, R., Corrales, L. R., Gao, F. & Weber, W. J. Signal variance in gamma-ray detectors—A review. *Nucl. Instrum. Methods Phys. Res. Sect. A* **565**, 637–649 (2006).
53. Wang, F., Zhang, T., Xie, R., Wang, Z. & Hu, W. How to characterize figures of merit of two-dimensional photodetectors. *Nat. Commun.* **14**, 2224 (2023).
54. Liu, J. et al. Flexible, printable soft-X-ray detectors based on all-inorganic perovskite quantum dots. *Adv. Mater.* **31**, 1901644 (2019).
55. Mescher, H. et al. Origami-inspired perovskite X-ray detector by printing and folding. *npj Flex. Electron.* **7**, 9 (2023).
56. Si, M. et al. Scaled indium oxide transistors fabricated using atomic layer deposition. *Nat. Electron.* **5**, 164–170 (2022).
57. Lin, J. et al. Printing of quasi-2D semiconducting β -Ga₂O₃ in constructing electronic devices via room-temperature liquid metal oxide skin. *Phys. Status Solidi I* **13**, 1900271 (2019).
58. Bell, J. et al. A 1.5-GHz 6.144T correlations/s 64 × 64 cross-correlator with 128 integrated ADCs for real-time synthetic aperture imaging. *IEEE J. Solid-State Circuits* **52**, 1450–1457 (2017).
59. Liang, H. et al. Flexible X-ray detectors based on amorphous Ga₂O₃ thin films. *ACS Photonics* **6**, 351–359 (2019).
60. Huang, W. C., Tseng, Z. C., Hsueh, W. J., Liao, S. Y. & Huang, C. Y. X-ray detectors based on amorphous InGaZnO thin films. *IEEE Trans. Electron Devices* **70**, 3690–3694 (2023).
61. Lakshmi Vineela, V., Praveen, P. A., Kanagasekaran, T., Kumar, C. N. & Narasimha Murthy, N. V. L. Direct X-ray detection using thin-film pentacene Schottky diodes. *J. Instrum.* **17**, P02024 (2022).
62. Chen, J. et al. High-performance X-ray detector based on single-crystal β -Ga₂O₃:Mg. *ACS Appl. Mater. Interfaces* **13**, 2879–2886 (2021).
63. Li, H. et al. Lead-free halide double perovskite-polymer composites for flexible X-ray imaging. *J. Mater. Chem. C* **6**, 11961–11967 (2018).
64. Su, K. et al. Highly-sensitive polycrystalline diamond X-ray dosimeter with hydrogen termination contacts. *IEEE Electron Device Lett.* **46**, 681–684 (2025).
65. Ruggieri, M. et al. Electrohydrodynamic jet-printed X-ray sensor based on iodide-exchanged lead(II) sulfide quantum dots. *ACS Appl. Mater. Electron. Mater.* **7**, 5549–5558 (2025).

Acknowledgements

This work was partially supported by the NSFC Grant (No. 91748206).

Author contributions

The project was designed and directed by J.L. Q.L., and R.F.L. developed the synthesis and printing procedure for quasi-2D Ga₂O₃ while also conducting the structure and properties measurements. R.F.L. led the X-ray detection devices fabrication and characterized the devices with contributions from X.Q.C. and C.H. R.F.L. analyzed the material and device characteristics and drafted the manuscript. Z.S.D. and M.H.G. helped to prepare schematics for the experimental setup for device and diagram of detector array imaging testing system. All authors discussed the results and commented on the manuscript.

Competing interests

The authors declare no competing interests.

Additional information

Supplementary information The online version contains supplementary material available at <https://doi.org/10.1038/s43246-025-01053-1>.

Correspondence and requests for materials should be addressed to Qian Li or Jing Liu.

Peer review information *Communications Materials* thanks the anonymous reviewers for their contribution to the peer review of this work. A peer review file is available.

Reprints and permissions information is available at <http://www.nature.com/reprints>

Publisher's note Springer Nature remains neutral with regard to jurisdictional claims in published maps and institutional affiliations.

Open Access This article is licensed under a Creative Commons Attribution-NonCommercial-NoDerivatives 4.0 International License, which permits any non-commercial use, sharing, distribution and reproduction in any medium or format, as long as you give appropriate credit to the original author(s) and the source, provide a link to the Creative Commons licence, and indicate if you modified the licensed material. You do not have permission under this licence to share adapted material derived from this article or parts of it. The images or other third party material in this article are included in the article's Creative Commons licence, unless indicated otherwise in a credit line to the material. If material is not included in the article's Creative Commons licence and your intended use is not permitted by statutory regulation or exceeds the permitted use, you will need to obtain permission directly from the copyright holder. To view a copy of this licence, visit <http://creativecommons.org/licenses/by-nc-nd/4.0/>.

© The Author(s) 2025